Scripta Materialia 184 (2020) 57–62

Contents lists available at ScienceDirect

Scripta Materialia

journal homepage: www.elsevier.com/locate/scriptamat

In-situ X-ray radiography of twinned crystal growth of primary $Al_{13}Fe_4$

S. Feng[a,*], Y. Cui[b], E. Liotti[a], A. Lui[a], C.M. Gourlay[b], P.S. Grant[a]

[a] Department of Materials, University of Oxford, Oxford, OX1 3PH, UK
[b] Department of Materials, Imperial College London, London, SW7 2AZ, UK

ARTICLE INFO

Article history:
Received 27 March 2020
Accepted 8 April 2020

Keywords:
Intermetallic compounds
Faceted growth
Growth twin
Twin plane re-entrant (TPRE) growth
In-situ X-ray radiography

ABSTRACT

The faceted growth of primary $Al_{13}Fe_4$ intermetallic compounds was studied using *in-situ* X-ray radiography in a solidifying Al-3Fe alloy. Microscopic twins were frequently observed in the growing intermetallics and were confirmed by post-solidification electron backscatter diffraction. A twin plane re-entrant growth mechanism was suggested, where repeated formation of re-entrant corners facilitated crystal growth along a preferential direction, forming elongated plates. In contrast, for intermetallics where this preferential growth was constrained by surrounding crystals, formation of layered twins perpendicular to the preferential direction was promoted and led to lower aspect ratios, known to be less deleterious to tensile properties.

During recycling of Al alloys, the accumulation of tramp impurities, Fe in particular [1], often leads to formation of coarse, faceted intermetallic compounds (IMCs) during solidification that degrade final product mechanical properties (e.g. tensile ductility and fatigue life [2]). Because it is costly to lower the Fe concentration and/or to use thermomechanical processing to sub-divide the IMCs [3], it is instead preferable to manipulate the morphology, size and distribution of the IMCs during solidification. Post-solidification microscopy and thermal analysis [2,4–15] have been used to study the IMCs, and more recently *in-situ* X-ray radiography [16–19] and tomography [20–22] have been adopted increasingly to investigate the dynamics of IMC growth. Using synchrotron radiography at 2 Hz, Wang *et al.* studied the growth of four secondary β-AlFeSi IMCs at a cooling rate of 0.33 Ks^{-1} [16]. There was initial rapid lateral growth with an IMC tip velocity of up to 100 μm s^{-1}, reducing to 10 μm s^{-1} towards the end of the growth. Similar trends of initial rapid growth followed by deceleration were reported by Terzi *et al.* [20] at 0.02 Ks^{-1} for β-AlFeSi using synchrotron tomography and by Bjurenstedt *et al.* [18] at 0.5 Ks^{-1} for α-Al(FeMnCr)Si using laboratory-based radiography, despite the differences in IMC crystal structure and cooling rate.

The related behaviour of faceted growth has been studied more extensively in semiconductor crystals such as Ge and Si, where frequently observed twinning is believed to facilitate the formation of low-energy sites for atom attachment that derives the anisotropic growth of faceted crystals [23–34]. This is known as the twin plane re-entrant (TPRE) mechanism, proposed by Wagner [23] and Hamilton and Seidensticker [24]. Growth twins on the closely-packed {111} facet of Ge crystals produce re-entrant corners (grooves in 3D) on the twin boundaries for preferential atom adsorption, which promote rapid growth along $\langle 11\bar{2}\rangle$ directions that results in a plate-like morphology [23,24].

It has been hypothesised that TPRE may be involved in the growth of Fe-rich IMCs, based on frequent microscopy observation of growth twins in β-Al_5FeSi and $Al_{13}Fe_4$ [11,35,36]. In the *in-situ* studies by Terzi *et al.* [20] and Bjurenstedt *et al.* [18], IMCs with branched morphologies were speculated to result from twinning, the detail of which could not be resolved due to limited imaging spatial and temporal resolution.

In this paper we investigate the growth dynamics and mechanism of faceted primary $Al_{13}Fe_4$ crystals in a hypereutectic Al-3Fe (wt%) alloy using *in-situ* X-ray radiography. With high spatial and temporal resolution, microscopic twins were frequently suggested, which were later confirmed by detailed post-solidification electron backscatter diffraction (EBSD) investigations. The repeated formation of twin plane re-entrant (TPRE) corners facilitated anisotropic growth along preferential directions, resulting in IMC platelets with a high aspect ratio of up to 10. In contrast, under some conditions the formation of layered, parallel twin platelets perpendicular to the preferential growth direction were promoted, leading to IMC thickening and a reduced final aspect ratio. We speculate that such insights may be used to contrive more mechanically benign IMC

---

* Corresponding author.
E-mail address: shikang.feng@materials.ox.ac.uk (S. Feng).

https://doi.org/10.1016/j.scriptamat.2020.04.010
1359-6462/

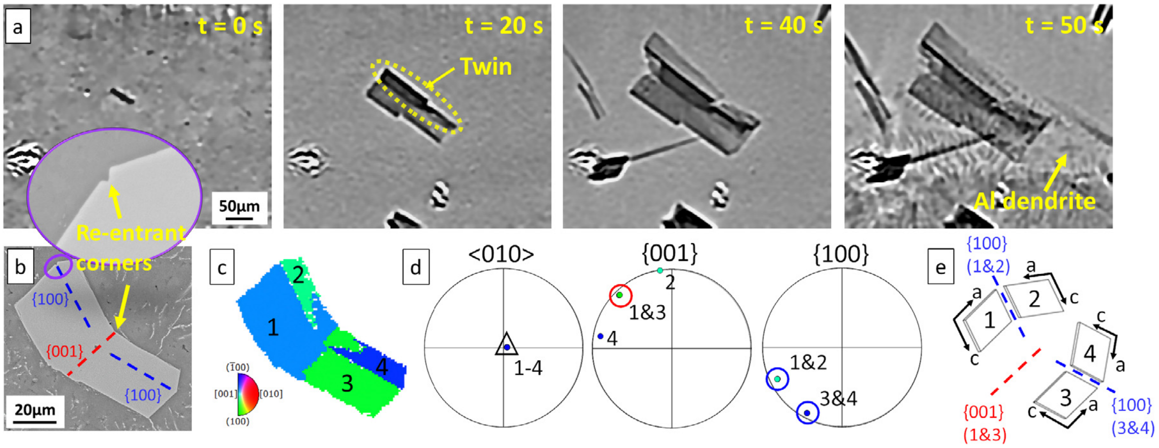

Fig. 1. (a) A radiograph sequence of primary $Al_{13}Fe_4$ crystals solidifying at 0.5 Ks^{-1}, showing microscopic twinning. The temperature at $t = 0$ at the position where the crystal first formed was 681°C. The real-time temperature at any time and position in the radiography field of view was estimated following the method in [19]. The error in estimating the temperature field was ± 1°C. (b) A secondary electron image of a twinned $Al_{13}Fe_4$ crystal in the same solidified sample as used in the synchrotron studies. The dashed lines indicate the twin planes, which in this case are perpendicular to the page, and the yellow arrows denote the re-entrant corners on the interfaces. Note that the size of the $Al_{13}Fe_4$ particle in (b) appeared smaller than the particle in (a), because the secondary electron image in (b) only showed an arbitrary exposed cross-section on a polished sample surface rather than the entire IMC. (c) An inverse pole figure of the crystal in (b) showing four different orientations. (d) Pole figures of the crystal in (b). (e) Unit cell wire frames that illustrate the four different orientations.

Table 1
A summary of the alloy, solidification conditions and characterisation techniques.

Alloy	Cooling rate (Ks^{-1})	Thermal gradient (Kmm^{-1})	Technique
Al-3Fe	Furnace cooling	≈ 0	EBSD
Al-3Fe	0.5	5	Radiography + EBSD
Al-3Fe	2	5	EBSD

morphologies in Al alloys, i.e. to facilitate the production of more “impurity-tolerant” alloys.

Synchrotron X-ray radiography of $Al_{13}Fe_4$ crystal growth was performed at beamline ID19, European Synchrotron Radiation Facility (ESRF), France. Details including sample preparation, experimental set-up and data analysis are provided in the Supplementary Materials. Overall, the size and growth velocity of 41 IMCs were measured within an error - based on repeating the measurement twice for all the 41 IMCs - of ± 4 μm and ± 5 μm s^{-1}, respectively.

For twinning investigations, samples from the synchrotron experiments were studied using a Zeiss Sigma field emission scanning electron microscope fitted with a Bruker e-Flash high-resolution EBSD detector. Details of EBSD sample preparation and pattern analysis are provided in the Supplementary Materials.

Table 1 summarises the alloy, solidification conditions and characterisation techniques.

Fig. 1(a) shows a radiograph sequence of primary $Al_{13}Fe_4$ crystals solidifying in Al-3Fe (wt%) at 0.5 Ks^{-1}. The crystals formed directly from the liquid. Later, Al dendrites formed around the growing IMCs ($t = 50$ s in Fig. 1(a)) towards the end of solidification. Very shortly afterwards, solidification completed via a eutectic reaction. Microscopic twin morphologies in many of the IMCs were suggested, for example as labelled in Fig. 1(a). EBSD investigations identified two types of twin (Fig. 1(b) to (e)). According to the inverse pole figure (Fig. 1(c)), there were four orientations in the crystal. The interface between 1 and 2 and between 1 and 3 coincided with the re-entrant corners on the facets, as highlighted in Fig. 1(b). Pole figures in Fig. 1(d) show that these four orientations shared the common monoclinic ⟨010⟩ direction. The common {001} plane (highlighted by a red circle in Fig. 1(d)) between 1 and 3 corresponded to the interface highlighted by a red dashed line in Fig. 1(b). The interface between 1 and 2 and between 3 and 4 is the {100} plane (highlighted blue circles), corresponding to the blue dashed lines in Fig. 1(b). The unit cell wire frames of these four orientations are plotted in Fig. 1(e). The twin type is identified as a 180° rotation along the common a-axis between 1 and 3 with {001} being the twin plane (i.e. {001} twinning), and a 180° rotation along the common c-axis between 1 and 2 (3 and 4) with {100} being the twin plane (i.e. {100} twinning). The presence of twins was also confirmed by EBSD in samples solidified under furnace cooling (cooling rate < 0.1 Ks^{-1}) and at 2 Ks^{-1}, as shown in Fig. S1 and Fig. S2 respectively in the Supplementary Materials. The clear *in-situ* observation (41 IMCs) combined with post-solidification EBSD (3 samples) confirmed earlier speculation of twinning [18,20].

Fig. 2(a) is a radiograph sequence showing typical growth of a millimetre-long primary $Al_{13}Fe_4$ crystal, where twin platelets (and re-entrant corners) appeared repeatedly along the preferential growth direction. Of 41 IMCs studied, this behaviour was quantitatively and qualitatively similar in 17 out of 41 observations. At time $t = 1$ s, a microscopic twin plate was observed on the slower growing facet of the crystal. At $t = 4$ s, a new plate formed at the re-entrant corner (or groove) between the twin platelets and propagated rapidly along the original growth direction ($t = 6$ s in Fig. 2(a)). A twin plate then appeared on this newly developed plate and gave rise to another re-entrant corner, and the IMC continued to propagate from this new re-entrant corner ($t = 12$ s). The process repeated ($t = 12$ s, $t = 16$ s and $t = 21$ s), allowing the crystal to keep growing along this preferential direction, and led to the highly elongated plate-like crystal shown at $t = 28$ s. The crystal then grew out of the field of view.

Fig. 2(b) and (c) show the evolution of the length, width and their velocities of the elongated IMC. In comparison with earlier work by Wang *et al.* [16], Terzi *et al.* [20], Bjurenstedt *et al.* [18] and Cai *et al.* [22], which showed nearly monotonic decay of IMC growth velocities with time, the preferential growth velocity (along the length) in the current work showed distinct periodic fluctuations. This was attributed to the relatively high temporal and spatial resolution (especially with the IMCs forming as primary phase). Combining the radiograph sequence and the velocity profile along the length, a peak velocity was always observed (Fig. 2(c)) following the development of a re-entrant corner (assessed as when a new plate first appeared at the re-entrant cor-

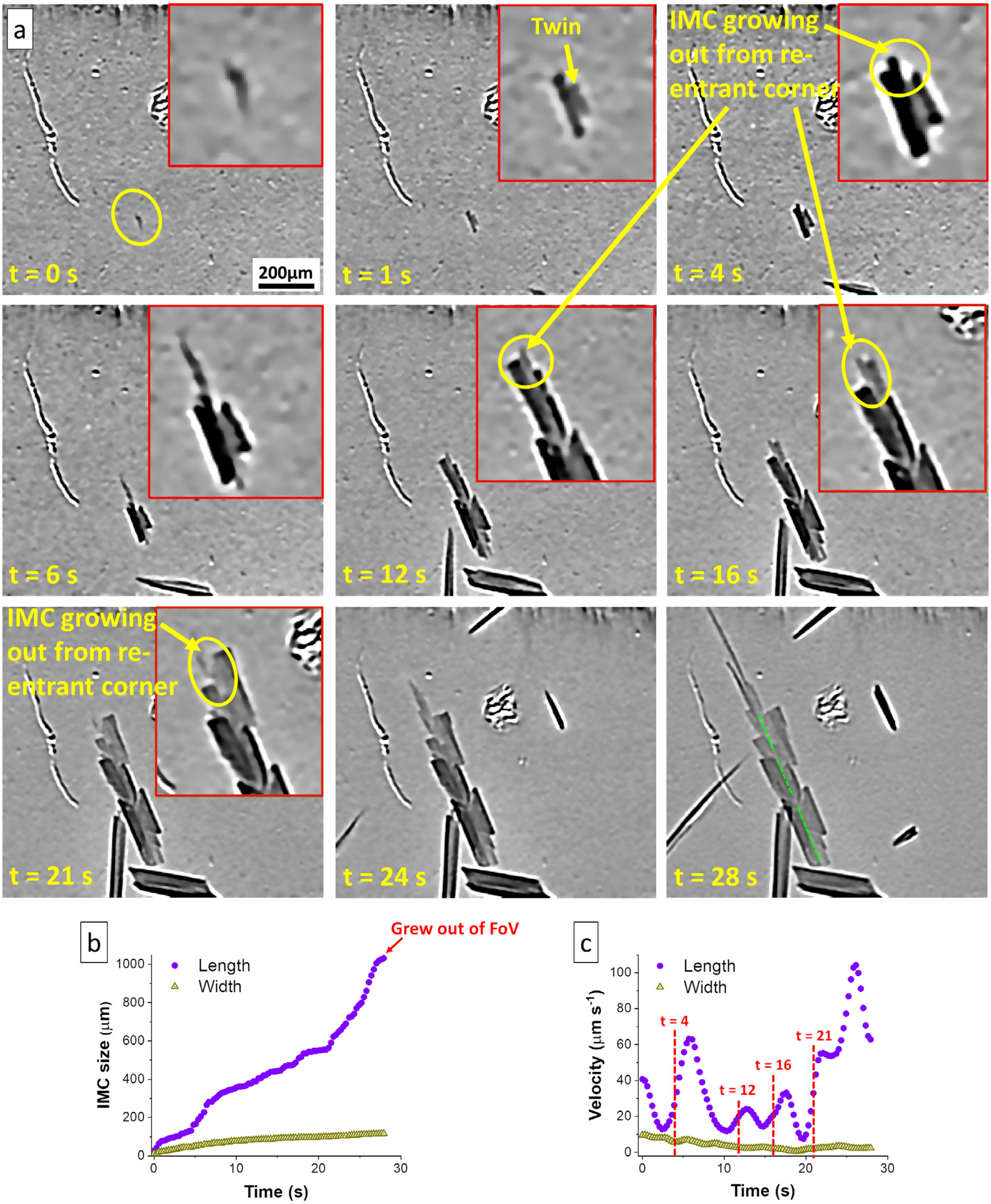

Fig. 2. (a) A radiograph sequence of growth of an elongated $Al_{13}Fe_4$ crystal at 0.5 Ks^{-1}, showing repeated suspected twin platelets and re-entrant corners. $t = 0$ was set at the beginning of the size measurement. Inset images with red frames provide a zoomed-in view. The temperature at $t = 0$ at the position where the crystal first formed was 677°C. The green dashed lines at $t = 28$ s highlight the boundaries between the microscopic twin platelets. (b) Evolution of the length and width. The IMC grew out of the field of view after $t = 28$ s. (c) Evolution of growth velocities along the length and width. The time when a new plate appeared at the re-entrant corners ($t = 4$ s, $t = 12$ s, $t = 16$ s and $t = 21$ s) is labelled.

ners: $t = 4$ s, $t = 12$ s, $t = 16$ s and $t = 21$ s, as labelled in Fig. 2(c)). This finding is in good qualitative agreement with the hypothesis proposed by Adam and Hogan [36] that the growth of elongated $Al_{13}Fe_4$ platelets was facilitated by a TPRE mechanism as a result of repeated formation of re-entrant corners.

Although the final length of the IMC was not able to be assessed, it grew to 1046 µm in 28 s at an average velocity of 37 µm s^{-1}, and had an aspect ratio of at least 9.

In contrast to this highly elongated IMC plate, there were also crystals containing layered platelets (24 out of 41 observations), with a much smaller final aspect ratio. Fig. 3(a) shows an exam-

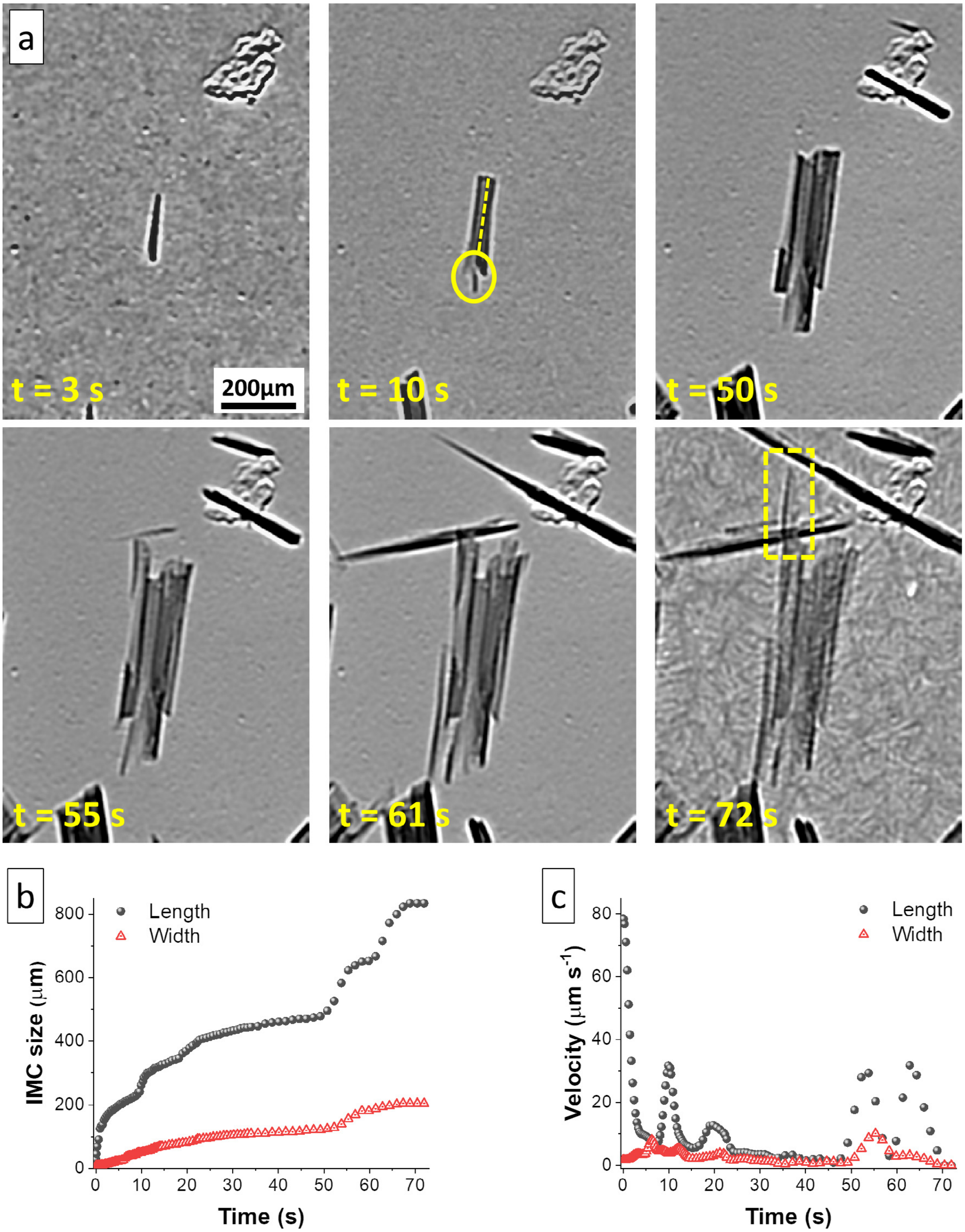

Fig. 3. (a) A radiograph sequence showing growth of a primary $Al_{13}Fe_4$ crystal containing layered platelets perpendicular to its preferential growth direction at 0.5 Ks^{-1}. The temperature at $t = 0$ at the position where the crystal first formed was 690°C. The yellow dashed line at $t = 10$ s highlights the boundary between two suspected twin platelets, and the circle highlights a new thin plate growing between. The dashed rectangle at $t = 72$ s highlights a thin IMC plate that overgrew the other platelets in the crystal but was stopped on impingement by a pre-existing crystal above it. (b) Evolution of the length and width of the crystal. (c) Evolution of growth velocities of the crystal.

ple, where the layered platelets appeared as a “bundle” of many parallel twins.

Growth of this crystal started at an initial velocity of 80 μm s^{-1} along the length (Fig. 3(c)). The velocity then decayed rapidly to below 10 μm s^{-1} in 3 seconds. In the meantime, a likely twin plate developed on the slower growing facet of the crystal, increasing the overall crystal width in the non-preferential direction. Following this, a new thin plate grew out from between the two platelets, at a peak velocity of 35 μm s^{-1} at $t = 10$ s. The yellow dashed line at $t = 10$ s in Fig. 3(a) highlights the boundary between the likely initial twin platelets, and the yellow circle highlights the thin plate growing between. Following this peak in growth velocity, there was then a longer period of slow growth: between $t = 23$ s and $t = 50$ s, the velocity along the preferential

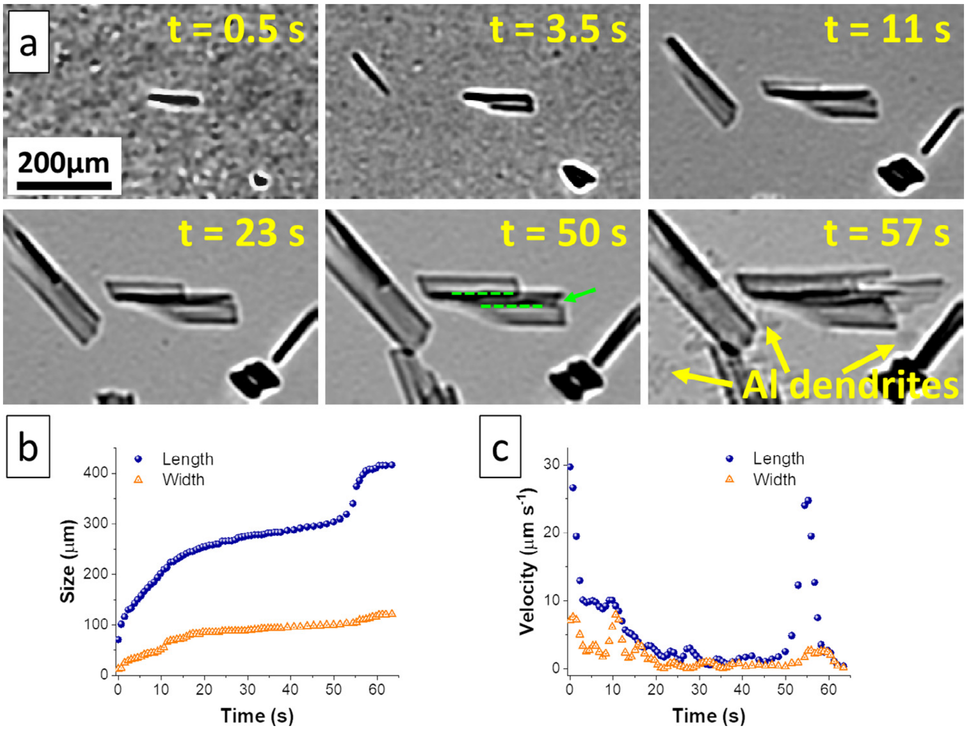

Fig. 4. (a) A radiograph sequence showing growth of a primary $Al_{13}Fe_4$ crystal containing layered platelets at 0.5 Ks^{-1}. The temperature at $t = 0$ at the position where the crystal first formed was 687°C. The green dashed lines at $t = 50$ s highlight the boundaries between the microscopic twin platelets, and the green arrow denotes a re-entrant corner. (b) Evolution of crystal length and width. (c) Evolution of growth velocities.

direction (i.e. the length) was only 2 to 3 μm s^{-1} (Fig. 3(c)), which was approximately equal to the velocity along the non-preferential direction. This period of "suppression" of preferential growth probably resulted from solute/solvent constraint due to the presence of other IMCs either "below" or "above", as shown in the field of view in Fig. 3(a) i.e. soft impingement of the Fe-denuded diffusion zones around each IMC. Towards the later stage of the growth (i.e. later stage of solidification), a thin IMC platelet rapidly overgrew the other platelets, as indicated by the yellow dashed rectangle at $t = 72$ s in Fig. 3(a). However, because of the presence of other IMC crystals that had grown in its path, the thin plate was halted by physical impingement. Compared with the elongated IMC in Fig. 2(a) where there were no other IMCs to constrain preferential growth, the crystal in Fig. 3(a) had a reduced length of 825 μm (compared with 1046 μm), an increased width of 205 μm (compared with 112 μm) and an aspect ratio reduced from > 9 to ~ 4.

Fig. 4(a) shows another crystal containing layered twin platelets, where the preferential growth was constrained by surrounding IMCs at an earlier stage, resulting in an even shorter length of 410 μm and further reduced aspect ratio of 3. The velocity along the length (Fig. 4(c)) followed a similar trend to that in Fig. 3(c), however with a lower initial velocity of 30 μm s^{-1} (compared with 80 μm s^{-1}) and a lower average velocity of 5 μm s^{-1} (compared with 11 μm s^{-1}). The reduced preferential growth velocity was because the crystal was aligned such that its preferential direction was constrained by other IMCs that formed in adjacent regions (Fig. 4(a)) and competed for solute (Fe). While the preferential growth was constrained, the width of the crystal, which was less constrained, grew via the formation of layered twin platelets, which became more recognisable as growth proceeded.

Table 2 summarises the average preferential growth velocities and aspect ratios measured from 41 IMCs. The crystals where anisotropic TPRE growth was not constrained (typical of Fig. 2) showed an average velocity of 23 ± 7 μm s^{-1} along their preferential direction and a final aspect ratio of 10 ± 2. The velocities are in a similar range to those reported by Wang *et al.* (34 ± 20 μm s^{-1} [16]) in the initial rapid growth stage (i.e. low constraint) for β-AlFeSi IMCs at 0.33 Ks^{-1}. Both are significantly higher than reported by Bjurenstedt *et al.* [18] at 0.5 Ks^{-1} for cubic α-Al(FeMnCr)Si (3.5 ± 0.5 μm s^{-1} and 2.5 ± 0.6 μm s^{-1}). The difference in growth velocities may reflect the difference in crystal symmetry between monoclinic and cubic IMCs, especially at little constraint. Where preferential growth was constrained (typical of Figs. 3 and 4) the average velocity reduced to 7 ± 3 μm s^{-1} and IMCs had a lower final aspect ratio of 3 ± 1 (i.e. more isotropic).

Table 2
A summary of the average growth velocity along the preferential direction and the final aspect ratio measured from 41 IMCs.

	Average velocity (μm s^{-1})	Final aspect ratio	No. of IMCs measured
Non-constrained	23 ± 7	10 ± 2	17
Constrained	7 ± 3	3 ± 1	24

Comparing Figs. 2(c), 3(c) and 4(c), a significant re-acceleration along the preferential direction was commonly observed towards the end of crystal growth (just before the appearance of the eutectic), when a thin platelet grew out from the bulk crystal, likely from a re-entrant corner. This occurred because the formation and growth of the Al dendrites as part of the terminal eutectic reaction rejected Fe into the surrounding liquid, resulting in a Fe-rich liquid environment to feed the growth of primary $Al_{13}Fe_4$ crystals (and also to form any additional eutectic $Al_{13}Fe_4$). In comparison, no re-acceleration towards the final stage was reported in previous *in-situ* studies [16,18,20], primarily due to low time resolution and that they were secondary IMCs that are more difficult to resolve in the presence of majority α-Al dendrites.

In Al-Si alloys the addition of chemical modifiers such as Sr and Na poison the re-entrant corners in Si crystals and the TPRE growth along $\langle 11\bar{2} \rangle$ directions is deactivated whilst layered {111} twins are promoted perpendicular to the preferential direction [28,29,37–39]. This contributes to thickening of the crystals via a combination of a restricted-TPRE mechanism [28] and an impurity-induced-twinning (IIT) mechanism [29,37]. The findings here and by analogy with the Al-Si system provide an inspiration that chemical modifiers might exist to provide some level of control over the growth morphology of otherwise highly elongated IMCs due to Fe pick-up in recycled Al alloys. Exploration of potential modifiers might provide an interesting avenue for high throughput computational materials design.

In summary, faceted growth of primary $Al_{13}Fe_4$ crystals was investigated during solidification of a hypereutectic Al-3Fe (wt%) alloy using *in-situ* X-ray radiography combined with post-solidification high-resolution EBSD. Growth twins were frequently present in $Al_{13}Fe_4$ crystals. Repeated formation of twin plane re-entrant corners facilitated the anisotropic preferential growth of the crystals and led to IMC platelets of high aspect ratio. In contrast, where the preferential TPRE growth was constrained, the formation of parallel twin platelets perpendicular to the preferential direction promoted thickening of IMCs and resulted in crystals of a much lower aspect ratio. Although this paper has identified TPRE growth as the principle mechanism for twinned $Al_{13}Fe_4$ crystals, other competing mechanisms may operate under different solidification conditions or in different alloys.

Declaration of Competing Interest

The authors declare that they have no known competing financial interests or personal relationships that could have appeared to influence the work reported in this paper.

Acknowledgements

This work was supported by EPSRC (UK) under grant number EP/N007638/1 (LiME - Liquid Metal Engineering). This work was enabled by synchrotron beamtime ID19 at European Synchrotron Radiation Facility (Experiment No. MA4063).

Supplementary material

Supplementary material associated with this article can be found, in the online version, at doi:10.1016/j.scriptamat.2020.04.010

References

[1] V. Kevorkijan, Mater. Tehnol. 47 (1) (2013) 13–23.
[2] G. Sha, K. O'Reilly, B. Cantor, J. Worth, R. Hamerton, Mater. Sci. Eng. A 304-306 (2001) 612–616.
[3] J. Cui, H.J. Roven, Trans. Nonferrous Met. Soc. China (English Ed.) 20 (11) (2010) 2057–2063.
[4] L.F. Mondolfo, Aluminum alloys : structure and properties, Butterworths, 1976.
[5] L. Backerud, E. Krol, J. Tamminen, Solidification characteristics of aluminium alloys, Skanaluminium, Universitetsforlaget AS, 1986.
[6] D. Liang, P. Korgul, H. Jones, Acta Mater. 44 (7) (1996) 2999–3004.
[7] Y. Wang, H. Jones, P. Evans, J. Mater. Sci. 33 (21) (1998) 5205–5220.
[8] Y. Wang, H. Jones, Metall. Mater. Trans. A 32 (5) (2001) 1251–1253.
[9] P. Ashtari, H. Tezuka, T. Sato, Mater. Trans. 44 (12) (2003) 2611–2616.
[10] H. Jones, Mater. Sci. Eng. A 413-414 (2005) 165–173.
[11] G. Sha, K. O'Reilly, B. Cantor, Mater. Sci. Forum 519-521 (2006) 1721–1726.
[12] H. Kamguo-Kamga, D. Larouche, M. Bournane, A. Rahem, Metall. Mater. Trans. A 41 (11) (2010).
[13] A. Verma, S. Kumar, P. Grant, K. O'Reilly, J. Alloys Compd. 555 (2013) 274–282.
[14] S. Kumar, K.A.Q. O'Reilly, Mater. Charact. 120 (2016) 311–322.
[15] S. Kumar, P.S. Grant, K.A.Q. O'Reilly, Metall. Mater. Trans. A 47 (6) (2016) 3000–3014.
[16] J. Wang, P.D. Lee, R.W. Hamilton, M. Li, J. Allison, Scr. Mater. 60 (7) (2009) 516–519.
[17] B. Kim, S. Lee, S. Lee, H. Yasuda, Mater. Trans. 53 (2) (2012) 374–379.
[18] A. Bjurenstedt, D. Casari, S. Seifeddine, R.H. Mathiesen, A.K. Dahle, Acta Mater. 130 (2017) 1–9.
[19] S. Feng, E. Liotti, A. Lui, S. Kumar, A. Mahadevegowda, K.A.Q. O'Reilly, P.S. Grant, Scr. Mater. 149 (2018) 44–48.
[20] S. Terzi, J.A. Taylor, Y.H. Cho, L. Salvo, M. Suery, E. Boller, A.K. Dahle, Acta Mater. 58 (16) (2010) 5370–5380.
[21] C. Puncreobutr, A.B. Phillion, J.L. Fife, P. Rockett, A.P. Horsfield, P.D. Lee, Acta Mater. 79 (2014) 292–303.
[22] B. Cai, A. Kao, P.D. Lee, E. Boller, H. Basevi, A.B. Phillion, A. Leonardis, K. Pericieous, Scr. Mater. 165 (2019) 29–33.
[23] R.S. Wagner, Acta Metall. 8 (1) (1960) 57–60.
[24] D.R. Hamilton, R.G. Seidensticker, J. Appl. Phys. 31 (7) (1960) 1165–1168.
[25] A. Hellawell, Prog. Mater. Sci. 15 (1) (1970) 3–78.
[26] K. Kobayashi, L.M. Hogan, Philos. Mag. A 40 (3) (1979) 399–407.
[27] O.A. Atasoy, F. Yilmaz, R. Elliott, J. Cryst. Growth 66 (1) (1984) 137–146.
[28] K.F. Kobayashi, L.M. Hogan, J. Mater. Sci. 20 (6) (1985) 1961–1975.
[29] S. Lu, A. Hellawell, J. Cryst. Growth 73 (2) (1985) 316–328.
[30] M. Shamsuzzoha, L.M. Hogan, J. Cryst. Growth 76 (2) (1986) 429–439.
[31] R. Wang, W. Lu, L.M. Hogan, J. Cryst. Growth 207 (1-2) (1999) 43–54.
[32] S. Hegde, K.N. Prabhu, J. Mater. Sci. 43 (9) (2008) 3009–3027.
[33] K. Fujiwara, Int. J. Photoenergy 2012 (2012) 1–16.
[34] J. Wang, Z. Guo, S.M. Xiong, Mater. Charact. 123 (2017) 354–359.
[35] M.H. Mulazimoglu, A. Zaluska, J.E. Gruzleski, F. Paray, Metall. Mater. Trans. A 27 (4) (1996) 929–936.
[36] C.M. Adam, L.M. Hogan, Acta Metall. 23 (3) (1975) 345–354.
[37] S. Lu, A. Hellawell, Metall. Trans. A 18 (10) (1987) 1721–1733.
[38] M. Timpel, N. Wanderka, R. Schlesiger, T. Yamamoto, N. Lazarev, D. Isheim, G. Schmitz, S. Matsumura, J. Banhart, Acta Mater. 60 (9) (2012) 3920–3928.
[39] X. Liu, Y. Zhang, B. Beausir, F. Liu, C. Esling, F. Yu, X. Zhao, L. Zuo, Acta Mater. 97 (2015) 338–347.